AIP Publishing Physics of Fluids ACCEPTED MANUSCRIPT
This is the author's peer reviewed, accepted manuscript. However, the online version of record will be different from this version once it has been copyedited and typeset.
PLEASE CITE THIS ARTICLE AS DOI: 10.1063/5.0268302

The three dimensional state of stratified shear instability in cold water

M. Stastna,[1] K. Bhavsar,[1] S. Hartharn-Evans,[2] and N. Castro-Folker[1]
[1)]*Department of Applied Mathematics, University of Waterloo*
[2)]*Department of Geography and Environmental Sciences, Northumbria University*

(*Electronic mail: mmstastn@uwaterloo.ca)

(Dated: 28 March 2025)

Stratified shear instability is one of the most widely studied routes to turbulence that occurs in natural waters. We report on simulations in the cold water regime relevant to late winter/early spring lakes, which is characterized by very small density differences and a nonlinear equation of state. The stratified shear instability in this regime achieves a three-dimensional state but it is not *a priori* clear that a substantial inertial subrange exists. We quantify the manner in which the three–dimensional state dissipates momentum and mixes scalars, and report on the nature of coherent structures in the flow with a focus on late times.

I. INTRODUCTION

The majority of natural waters are density stratified over at least some portion of the calendar year. The primary forcing of such waters can be mechanical (e.g. by the wind) or buoyancy-related (e.g. by solar radiation). In the late winter/early spring many mid and high latitude lakes are ice covered, meaning that mechanical forcing by the wind is precluded. Such lakes are also often observed to have an inverse stratification, with cold water overlying warmer water. This is possible due to the nonlinear nature of the equation of state for freshwater, which predicts a maximum density near a temperature of four degrees Centigrade. Since the increasing solar radiation associated with the coming Spring can at least partially penetrate through the ice cover, convective instability can be induced by warming. For example, well–developed overturns were observed under ice in Lake Simcoe, Canada by Yang *et al*[1]. Since the overlying ice cover is spatially varying, a number of scenarios have been identified and simulated for buoyancy–induced lateral motions in such lakes ([2,3]). Large eddy simulations of the larger scale organization of radiatively driven convection in such lakes have also been carried out in ([4]).

All the simulations described above focus on situations in which many features evolve simultaneously. A different point of view follows the stratified shear instability literature (e.g.[5]) by considering a single transition route to turbulence in detail. It is well-known that stratified shear instabilities form a primary instability, the well-known Kelvin–Helmholtz billow ([6]), and that this is followed by a secondary instability ([7,8]) that subsequently leads to a breakdown to a three–dimensionalized state. In what is now classical work, Caulfield and Peltier[5] showed that the rate of mixing greatly increases during the three–dimensionalization of the instability. In the subsequent decades, computational fluid dynamicists have largely sought to increase the Reynolds number of the shear flow simulated (e.g.[9]) with a view to answering question of whether there is a universal value of mixing efficiency in natural waters ([10,11]).

The largely quiet world of under ice flow in lakes offers an alternative portion of parameter space to explore. Since the ice precludes the primary input of mechanical energy via wind, the challenge is no longer reaching a high Reynolds number. Moreover, buoyancy driven motions are expected to also be relatively slow, since the maximum density difference is bounded above by $\Delta\rho \approx 0.1$ kg m^{-3}. Instead, what is important is the realistic modeling of what is a nonlinear, and possibly non-monotonic density versus temperature curve. The case of so–called strong cabbeling, in which temperatures both above and below the temperature of maximum density are observed has been documented in lakes for decades ([12,13]). From a theoretical/numerical point of view, the problem was considered by Hanson *et al*[14], who showed that the instability was a hybrid of shear instability in the plane of shear, and Rayleigh Taylor instability in the plane perpendicular to the shear. In other words the onset of instability is three-dimensional and two-dimensional simulations, even when carefully analyzed[15], need to be taken with a grain of salt. The work of Hanson *et al* was extended in Grace *et al*[16] to a deeper domain, a broader parameter regime and a longer integration time. It was found that after a period of strong mixing, a quasi-stable state in which a low-energy three-dimensional flow lies underneath a quiescent layer is achieved. This implies that any mixing of material from the lake bottom, could not reach the near surface region where it could, for example, provide nutrients for under–ice algae.

As impressive as strong cabbeling is, the nonlinearity of the equation of state has significant dynamical effects even if the fluid is strictly below the temperature of maximum density (as would be the case during the so–called winter 1 period[17]). For example, Castro-Folker *et al*[18] showed that the nonlinearity of the equation of state yields fundamental differences in the manifestation of lobe cleft instabilities for rising and sinking gravity currents.

We thus consider the instability of shear flow in a fluid strictly below the temperature of maximum density. In a laboratory setting it is the temperature that would be specified, hence we choose to specify a temperature profile along with a shear profile. The instability onset and the question of what role the small density differences have in it has been addressed in a companion publication ([19]). This has primarily been done through comparing temperature profiles and evolution of kinetic energy leading up to the development of three-dimensional flow. Herein we seek to characterize the three-dimensionalized state of the instability using tools often associated with turbulence theory (e.g. the $Q-R$ variables). We

AIP Publishing Physics of Fluids ACCEPTED MANUSCRIPT
This is the author's peer reviewed, accepted manuscript. However, the online version of record will be different from this version once it has been copyedited and typeset.
PLEASE CITE THIS ARTICLE AS DOI: 10.1063/5.0268302

do this because despite reaching a fully three-dimensionalized state, the mature state of the instability never achieves a well–developed inertial subrange (e.g. there is no range of scales for which dissipation is negligible). Moreover, there has been the suggestion in the literature[20] that upon reaching maturity a stratified shear instability returns to what is referred to as the state of marginal stability, characterized by a gradient Richardson number near 0.25. Whether this is the Richardson number for horizontally averaged flow, or something more local is an open question. Recent work on stratified wakes[21] suggests it is possible to define a "local" Richardson number based on a filtering procedure and to characterize threshold behavior in the flow based on it. Moreover, this works suggests that marginal stability may be more generic than any particular route to three-dimensionalizing.

The remainder of this manuscript is organized as follows. First the governing equations, numerical methods, and derived quantities used for analysis are defined. Next the general flow evolution as the fully three-dimensionalized flow is achieved is described. This is followed by a detailed discussion of the $Q-R$ variables. The results conclude with a discussion of how the quasi-turbulent state is maintained at late times. The manuscript concludes with a Discussion section.

II. METHODS

A. Governing equations

The simulations reported on in the following were performed using the pseudo-spectral collocation method solver for the stratified, incompressible Navier-Stokes equations SPINS[22]. The Boussinesq approximation is used throughout, and the governing equations are given by Kundu[6]:

$$\frac{D\vec{u}}{Dt} = \frac{-1}{\rho_0}\nabla p - \frac{\rho'(T)}{\rho_0} g\hat{k} + \nu\nabla^2\vec{u}, \tag{1}$$

$$\nabla\cdot\vec{u} = 0, \tag{2}$$

$$\frac{DT}{Dt} = \kappa\nabla^2 T, \tag{3}$$

where $\vec{u} = (u,v,w)$ is the velocity, p denotes the pressure field, ρ_0 is a reference density (1000 kg m^{-3}), ρ' denotes the density perturbation around the reference value (i.e. $\rho(x,y,z,t) = \rho_0 + \rho'(x,y,z,t)$), ν and κ are the kinematic viscosity of water, and thermal diffusivity, respectively, g is the gravitational acceleration, t is time, and T denotes the temperature field. The unit vector in the vertical direction is denoted by $\hat{k}$. The origin is located at the bottom left of the numerical tank, with the x-axis pointing streamwise, the z-axis pointing upwards and the spanwise y-axis determined via the right-hand rule. The values of the constants used in these governing equations are given in table I.

While the results are insensitive to the precise form of the equation of state used (e.g. a quadratic equation of state), simulations are reported using the form in Brydon *et al.*[23]. This equation is a seven-term polynomial that is cubic in temperature and linear in salinity (though the salinity is fixed as zero in all simulations reported herein). The temperatures of water are kept between $T_0 = 0^\circ C$ and $T_{\max} = 3.5^\circ C$ (which is the shifted temperature of maximum density) so as to stay within the monotonic branch of the equation of state. Work on the onset of instability and the sensitivity of such an instability to the various parameters is reported in the companion paper[19].

B. Dimensionless parameters

The numerical simulations are performed using dimensional equations at the laboratory scale. In order to provide a non-dimensional context, we will consider the height of the tank, H (in meters), to be the characteristic length scale, L. The characteristic velocity scale, U, will be given by the maximum initial horizontal velocity, u_0. Time is scaled by the advective time scale L/U. Finally, the temperature is scaled to values between -1 and 0 using the following non-dimensionalization,

$$\tilde{T} = \frac{T - T_{\max}}{T_{\max} - T_0}. \tag{4}$$

Scaling the governing equations by these parameters, leads to a form in terms of standard dimensionless parameters: Reynolds number (Re), Péclet number (Pe) and Froude number (Fr),

$$\vec{\nabla}\cdot\vec{u} = 0, \tag{5}$$

$$\frac{D\vec{u}}{Dt} = -\vec{\nabla}p + \frac{1}{\mathrm{Re}}\nabla^2\vec{u} - \frac{1}{\mathrm{Fr}^2}R(T)\hat{k}, \tag{6}$$

$$\frac{DT}{Dt} = \frac{1}{\mathrm{Pe}}\nabla^2 T. \tag{7}$$

Here, $R(T)$ is the nondimensionalized equation of state[14] and the tildes have been dropped. Tildes will also be dropped in all figures below.

The Atwood Number is given by:

$$\mathrm{At} = \frac{\rho_{max} - \rho_{min}}{\rho_{max} + \rho_{min}} = 3.29\times 10^{-5}, \tag{8}$$

and the representative values of the other dimensionless numbers are,

$$Re = \frac{UL}{\nu} \approx 1000, \tag{9}$$

$$Pe = \frac{UL}{\kappa} \approx 10000, \tag{10}$$

$$Fr = \frac{U}{\sqrt{gL}} \approx 0.01. \tag{11}$$

Note that the Froude number as written is small due to the use of g. This is the result of defining the Froude number as a

ACCEPTED MANUSCRIPT
Physics of Fluids
AIP Publishing
This is the author's peer reviewed, accepted manuscript. However, the online version of record will be different from this version once it has been copyedited and typeset.
PLEASE CITE THIS ARTICLE AS DOI: 10.1063/5.0268302

g (ms^{-2})	ρ_0 ($kg\ m^{-3}$)	ν (m^2s^{-1})	κ (m^2s^{-1})	u_0 (ms^{-1})
9.81	1000	10^{-6}	1.43×10^{-7}	0.01

TABLE I. Parameters for the governing equations

direct ratio of terms in the governing equations. If we instead use the reduced gravity, $g' = g\Delta\rho/\rho_0$, we find

$$Fr_{internal} = \frac{U}{\sqrt{g'L}} \approx 100 \tag{12}$$

and that the flow is strongly supercritical (due to the very weak stratification).

C. Design of Numerical Experiments

The numerical tank employed has dimensions $L_x = 0.512$ m, $L_y = 0.128$ m and $L_z = 0.128$ m. The number of grid points in each dimension is $N_x = 512$, $N_y = 128$, $N_z = 128$, which results in a 1 mm resolution in all directions. Although the flow reaches a three-dimensionalized state, it is unclear whether estimates of the viscous dissipation scale based on isotropic, homogeneous turbulence are relevant. We thus prefer to set the resolution based on a physical scale. Details of the mature distribution of dissipation are discussed in the results section below. Free slip boundary conditions were applied at the upper and lower boundaries, with regular grid spacing in all dimensions and periodic boundary conditions in the x and y directions.

The temperature profile profile is initialized as

$$T = T_0 + \frac{1}{2}\Delta T\left(1 - \tanh\left(\frac{z - z_{center}}{L_{temp}}\right)\right). \tag{13}$$

while the initial horizontal velocity profile (u) is initialized as,

$$u = u_0 \tanh\left(\frac{z - z_{center}}{L_{shear}}\right). \tag{14}$$

Here L_{shear} is the thickness of the shear layer and L_{temp} is the thickness of the stratified layer. For the experiments performed in this paper, we take $L_{shear} = L_{temp} = 0.01$m, and $z_{center} = 0.064$m is the midpoint of the shear layer as well as the stratified layer. The type of instability developed in a stratified shear flow depends on the scale ratio[24] $R = L_{shear}/L_{temp}$, which in this case is 1. The resulting instability is thus expected to be of Kelvin-Helmholtz type, as opposed to Holmboe type. The simulation is initialized with a standard additive white noise component at a level of 10^{-3} in order to trigger an instability.

The nondimensional initial profiles are indicated by the blue curves in Figure 1. The velocity curve has been shifted so it is centered at -0.5 in order to use a common set of axes in the three panels. The bulk Richardson Number for these initial profiles is $J = (\Delta\rho g L_{shear})/(\rho_0(2u_0)^2) \approx 0.016$.

D. Derived Quantities

Following standard practice in fluid mechanics ([6]), the kinetic energy is defined without the factor ρ_0,

$$KE(x,y,z,t) = \frac{1}{2}(u^2 + v^2 + w^2). \tag{15}$$

We define the vector $\vec{u}_{3D}$ as the velocity vector with the spanwise average removed,

$$\vec{u}_{3D} = \vec{u} - \langle\vec{u}\rangle_y = (u_{3D}, v_{3D}, w_{3D}), \tag{16}$$

and use this to further define the 3D kinetic energy as discussed widely in the literature, e.g.[25],

$$KE_{3D}(x,y,z,t) = \frac{1}{2}(u_{3D}^2 + v_{3D}^2 + w_{3D}^2). \tag{17}$$

The enstrophy, split into components is written using the vorticity

$$\vec{\omega} = (\omega_x, \omega_y, \omega_z) = \nabla \times \vec{u} \tag{18}$$

as follows

$$\Omega = \Omega_x + \Omega_y + \Omega_z = \frac{1}{2}\left(\omega_x^2 + \omega_y^2 + \omega_z^2\right). \tag{19}$$

The evolution of vorticity is given by (Ref.[6])

$$\frac{D\vec{\omega}}{Dt} = (-\rho_y g, \rho_x, g, 0) + \vec{\omega}\cdot\nabla\vec{u} + \nu\nabla^2\vec{\omega}. \tag{20}$$

The term $\vec{\omega}\cdot\nabla\vec{u}$ is only non-zero in three-dimensions and represents the ability of the flow to spontaneously generate vorticity via vortex stretching and tilting. The term $(-\rho_y g, \rho_x, g, 0)$ is the baroclinic vorticity production, in its simplified form appropriate for the Boussinesq approximation. The governing equation for the enstrophy, $\Omega = (1/2)\vec{\omega}\cdot\vec{\omega}$, can be written using index notation:

$$\begin{aligned}\frac{D\Omega}{Dt} =& -\omega_k\varepsilon_{ijk}\rho_{,i}g_j \\ &+ \omega_i\omega_j e_{ij} \\ &- \nu\varepsilon_{ijk}\omega_{i,j}\varepsilon_{ijk}\omega_{i,j} \\ &+ \nu\left(\varepsilon_{ijk}\omega_j[\varepsilon_{mnk}\omega_{m,n}]\omega_k\right)_{,i}\end{aligned} \tag{21}$$

where ε_{ijk} is the alternating tensor. The two terms of interest in the discussion presented below are

$$ES = \omega_i\omega_j e_{ij}, \tag{22}$$

ACCEPTED MANUSCRIPT
Physics of Fluids
AIP Publishing
This is the author's peer reviewed, accepted manuscript. However, the online version of record will be different from this version once it has been copyedited and typeset.
PLEASE CITE THIS ARTICLE AS DOI: 10.1063/5.0268302

which represents the production and destruction of enstrophy by stretching and compression, and

$$EB = -\omega_k \varepsilon_{ijk} \rho_{,i} g_j, \tag{23}$$

which represents the production and destruction of enstrophy by baroclinic torques.

The viscous dissipation, which defines the irreversible transfer of mechanical energy into heat is defined as

$$\phi = 2\mu e_{ij} e_{ij} \tag{24}$$

where $\mu = \nu\rho_0$ is the dynamic viscosity, and e_{ij} is the rate of strain tensor. The repeated indices imply that the viscous dissipation is proportional to the double contraction of the rate of strain tensor with itself. The viscous dissipation is assumed to be high in regions with significant three-dimensionalization or transition to a three-dimensionalized state.

The third set of derived quantities of interest consists of tools developed to identify regions with coherent vortices[26,27]. The computation follows a three step process. First the velocity gradient matrix is computed as

$$A_{ij} = \frac{\partial u_i}{\partial x_j}.$$

Second, its eigenvalues $(\lambda_1, \lambda_2, \lambda_3)$ are computed. Third, the coefficients of the cubic characteristic polynomial, which are necessarily invariant, are derived from the following relations:

$$\begin{aligned} P &= \lambda_1 + \lambda_2 + \lambda_3 = \text{trace}(A_{ij}) \\ Q &= -\frac{1}{2}\left(\lambda_1^2 + \lambda_2^2 + \lambda_3^2\right) = \frac{1}{2}\left(\Omega - e_{ij}e_{ij}\right) \\ R &= \frac{1}{3}\left(\lambda_1\lambda_2\lambda_3\right) = \det(A_{ij}), \end{aligned} \tag{25}$$

where λ_1, λ_2, and λ_3 are the roots of the characteristic polynomial, Ω is the enstrophy, and e_{ij} is the rate of strain tensor[26–28]. Because $\text{trace}(A_{ij}) = \nabla \cdot \vec{u}$, the incompressibility condition implies $P = 0$.

Notice that when Q is expressed in terms of e_{ij} and Ω, it represents a balance between strain and rotation. That is to say, the flow is enstrophy-dominated when Q is large-amplitude and positive, and the flow is strain-dominated when Q is large-amplitude and negative.

R can be used with Q to classify flow topology. To be precise, Chong *et al.*[28] derived a topological transition curve that delineates the R-Q plane into regions where enstrophy or strain dominate in incompressible flows. This topological transition curve is defined as the set of points where the quantity,

$$D = Q^3 + \frac{27}{4}R^2, \tag{26}$$

takes a value of zero. Points where $D > 0$ are said to be enstrophy-dominated, and points where $D < 0$ are said to be strain-dominated. This categorization is motivated by the relationship between the eigenvalues of A_{ij} and the local structure of streamlines. Namely, $D > 0$ at a point results in A_{ij} having all real eigenvalues, and $D < 0$ results in A_{ij} having a pair of complex eigenvalues. The significance of this criterion is that two complex eigenvalues at a point implies the streamlines to possess locally helical structure[26–28].

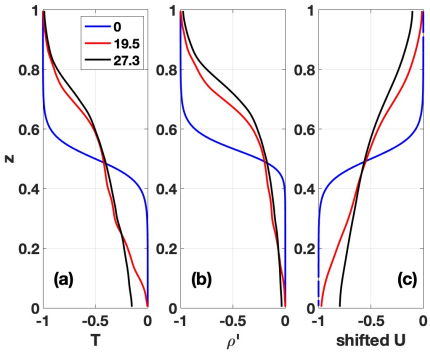

FIG. 1. The domain horizontally averaged profiles scaled to lie on $[-1,0]$ at $\tau = 0$ (blue), 19.53 (red) and 27.34 (black) of (a) temperature, (b) $\rho' = \rho - \rho_0$ (c) streamwise component of velocity (u).

III. RESULTS

A. General Flow Evolution

While the focus in the following will be on the detailed dynamics, it is important to keep in mind that the bulk effect of the instability is to mix both the passive and active scalars as well as the momentum. The vertical momentum profile (rightmost panel in Figure 1) reaches a broad state, which to leading order could be considered linear in z. Both the temperature and excess density profiles (left and middle panels in Figure 1, respectively) maintain a transition region structure. However, the center of this transition region shifts upward. The weakest mixing of density occurs near the top of the domain.

The manner in which the system reaches the averaged state shown in Figure 1 follows a relatively standard Kelvin-Helmholtz paradigm. Figure 2 shows the temperature field as the instability sets in (panel (a)), billows pair (panels (b) and (c)) and true three-dimensionalization begins to set in (panel (d)). The three-dimensionalization of the flow is initially small but prominent in both the billow cores and the braids connecting them at $\tau \approx 8$. After pairing has occurred, the three-dimensionalization grows within the paired billow core and develops into a fully 3D flow at $\tau \approx 18$. Figure 3 shows three x-y slices at the locations indicated by blue lines in the x-z plot shown in panel (a). It is clear that the intensity of three-dimensionalization varies in the spanwise direction. For further discussion of the onset of three-dimensionalization see Bhavsar, Stastna, and Castro-Folker [19].

Due to the extremely small value of the Atwood number the three dimensionalization process is best quantified using the changes in the kinetic energy and its counterpart that removes the spanwise average, KE_{3D}. Figure 4(a) shows the decay in total kinetic energy (black curve) and the increase in KE_{3D} (red curve) from about $\tau = 15$ onward. It is worth noting that the in this modest Reynolds number regime the

ACCEPTED MANUSCRIPT
Physics of Fluids
AIP Publishing
This is the author's peer reviewed, accepted manuscript. However, the online version of record will be different from this version once it has been copyedited and typeset.
PLEASE CITE THIS ARTICLE AS DOI: 10.1063/5.0268302

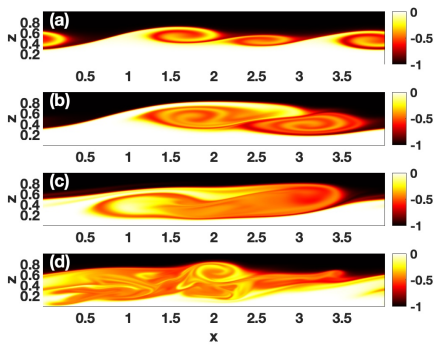

FIG. 2. Slice of the temperature field at $\tau =$ (a) 7.81, (b) 11.72,(c) 15.62, (d) 19.53.

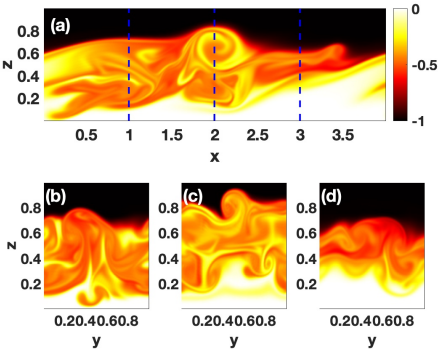

FIG. 3. Slices of the temperature field at $\tau = 19.53$ (a) $x-z$ (b),(c),(d) y-z plane at the blue dashed lines indicated on panel (a). All panels use the color range indicated by the colorbar for panel (a).

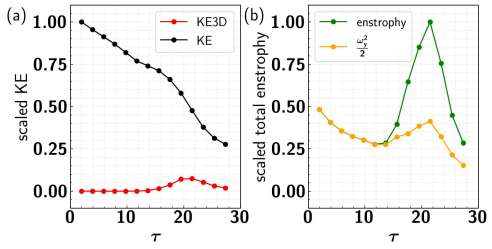

FIG. 4. (a) Total KE (black) and total KE_{3D} (red) scaled by the maximum of the total KE versus time. (b) Total enstrophy (green) and total $\omega_y^2/2$ (orange) scaled by the maximum of the total enstrophy versus time.

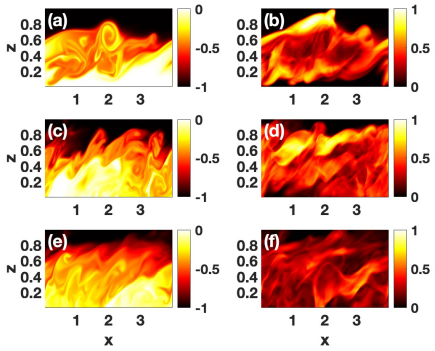

FIG. 5. Left column: slices of the temperature at $y = 0.074$, Right column: standard deviation of the temperature field. (a),(b) $\tau =$ 19.53, (c),(d) $\tau = 23.43$, (e),(f) $\tau = 27.34$. (a,c,e) have been scaled to lie on $[-1,0]$ as in Figure 1, (b,d,f) have been scaled to lie on $[0,1]$. All panels thus show the geometric distribution.

total kinetic energy decays throughout the simulation, though the rate of decay clearly increases as three-dimensionalization sets in. Panel (b) offers a different perspective using the total enstrophy (red) and the enstrophy based on the y component of vorticity only (orange). It can be seen that during the three-dimensionalization the enstrophy grows by over 100% of its initial value, peaking at around $\tau = 19.53$ and decaying thereafter. The in–plane component of enstrophy has a much smaller increase over this period, implying that three-dimensional motions, and their spatial gradients, are essential over this time period.

The state of the temperature field during the full three-dimensionalized period is shown in Figure 5. The left column shows a slice at $y = 0.5$, while the right column shows the spanwise standard deviation. At $\tau = 19.53$, the peak of KE_{3D} we see that the temperature field has a prominent vortex at the center of the domain. This vortex has not fully three-dimensionalized since the standard deviation field in panel (b) is dominated by horizontal layers near the bottom and top of the domain. As the fluid evolution proceeds, the horizontal layer of strong standard deviation near the bottom decays, while the layer near the top is marked by multiple small vortices. For late times the standard deviation is markedly decreased and near the top of the domain a black region of nearly homogeneous fluid is observed.

Despite the low Atwood number, buoyancy effects and the nonlinearity of the equation of state do modify the observed state[19]. Figure 6 shows a slice of the temperature (a) and density fields (b). It can be seen that the nonlinearity of the equation of state manifests by decreasing the strength of the gradients in the broad central region (i.e. panel (b) is dominated by orange-red whereas panel (a) is not dominated by specific colors).

Smyth and colleagues[20] have argued that on large scale (e.g.

ACCEPTED MANUSCRIPT
Physics of Fluids
AIP Publishing
This is the author's peer reviewed, accepted manuscript. However, the online version of record will be different from this version once it has been copyedited and typeset.
PLEASE CITE THIS ARTICLE AS DOI: 10.1063/5.0268302

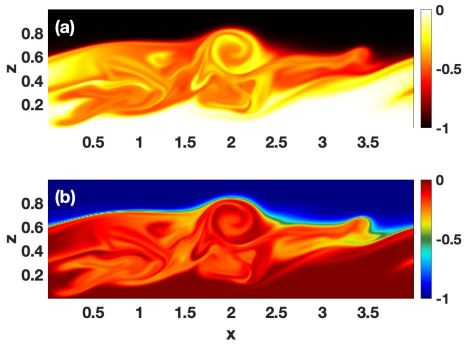

FIG. 6. Slice of the temperature (a) and excess density (b) fields at $\tau = 19.53$ and $y = 0.074$ showing the importance of the nonlinear equation of state.

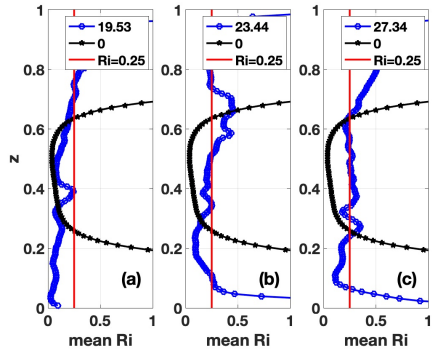

FIG. 7. Plots of the gradient Richardson number based on the horizontally averaged density and streamwise velocity profiles. The critical value of $Ri = 0.25$ is indicated by a red vertical line and the initial Ri versus z profile is shown in black. (a) $\tau = 19.52$ s, (b) $\tau = 23.43$, (c) $\tau = 27.34$.

the Equatorial Undercurrent) stratified shear flows naturally evolve toward a state of marginal stability marked by a vertical profile of gradient Richardson number clustered around the critical value of $Ri = 0.25$. For strongly-stratified shear flows, Salehipour *et al.*[29] attribute marginal instability to the Holmboe wave instability, since Kelvin-Helmholtz overturns result in mixing too vigorous to remain marginally unstable. While $Ri < 0.25$ is a necessary, but not sufficient, condition for linear instability, we wanted to see to what extent our flow tended toward marginal instability. Figure 7 shows the profiles of the gradient Richardson number as a function of z at $\tau = 19.53$, 23.43 and 27.34 (blue curves). The fraction of the water column for which $Ri < 0.25$ is $(0.72, 0.47, 0.34)$ for the three times shown. The initial Ri profile is shown as a black curve in each panel. The critical value of $Ri = 0.25$ is indicated by a red curve. It can be seen that a small region of marginal stability is evident between $z = 0.3$ and 0.6 by $\tau = 23.43$. The region of marginal stability expands to $0.1 < z < 0.65$ by $\tau = 27.34$. Thus even in this modest energy, extremely low Atwood number state the flow does reach a partial marginally stable state, produced by Kelvin-Helmholtz overturning. However, the region near the top boundary, which is largely unmixed (as already noted by Hanson *et al.*[14]) never reaches a marginal state.

B. Coherent Structures

The derived Q field is often used to identify coherent structures (i.e. coherent vortices) in transitional and turbulent flows. Figure 8 shows two perspectives on these coherent structures at $\tau = 19.53$ (panels a,b) and 27.34 (panels c,d). It can be seen that at $\tau = 19.53$ the Q field is quite busy with a single spanwise oriented region (a vortex) between $x = 1.5$ and 2.5 matching that highlighted in figure 6 (panel a). Streamwise–oriented isoregions wrap around the spanwise oriented region. At the later time, the regions marked as "coherent" vortices by the Q field are much thinner, and are almost exclusively (apart from the feature near $x = 4$) streamwise oriented. Coherent vortex structures appear to be preferentially found near the boundary of the unmixed fluid found near the upper boundary.

Since Q is an abstract quantity, we examined distributions of the physics–grounded viscous dissipation and the vortex stretching and tilting term using threshold-based co-occurrence of variables (e.g.[30]). Figure 9 shows shaded slices of the temperature field at $\tau = 19.53$ (left hand panels (a,b,c,d)) and 27.34 (right hand panels (e,f,g,h)). Superimposed on the plots are regions greater than 15% of the maximum value of viscous dissipation in magenta, and the vortex stretching and tilting term in blue. Regions with both quantities above their respective thresholds are shaded in green. At the earlier time (left), the coherent vortex near $x = 2$ dominates some but not all slices. The later time, like the Q field in Figure 8, highlighted regions show features dominated by thin streamwise streaks. This indicates that general conclusions based on Q carry over to the viscous dissipation and vortex stretching field. It is however interesting that in all of our panels there are clear regions in which only one of viscous dissipation or vortex stretching takes on high values.

To identify whether the properties of the $Q-R$ distribution agree with the actual observations of vortex stretching, the quantity ES defined by equation (22), is explored using the well-known $Q-R$ "ice cream cone" plots in Figures 10 and 11. The two figures consist of a shaded plot of the $\log_{10}$ of the probability density in $Q-R$ space, with colours saturated on $[-7, -4]$. The topological transition, $D = 0$, curve is superimposed in black and the quadrants of $Q-R$ space are denoted by dashed yellow lines. The 50% largest values of the enstrophy stretching term are shown as white points (top 10% further accentuated as green crosses), which theory would suggest should fall in the first and third quadrants above the topological transition curve. The 50% most negative val-

ACCEPTED MANUSCRIPT
Physics of Fluids
AIP Publishing
This is the author's peer reviewed, accepted manuscript. However, the online version of record will be different from this version once it has been copyedited and typeset.
PLEASE CITE THIS ARTICLE AS DOI: 10.1063/5.0268302

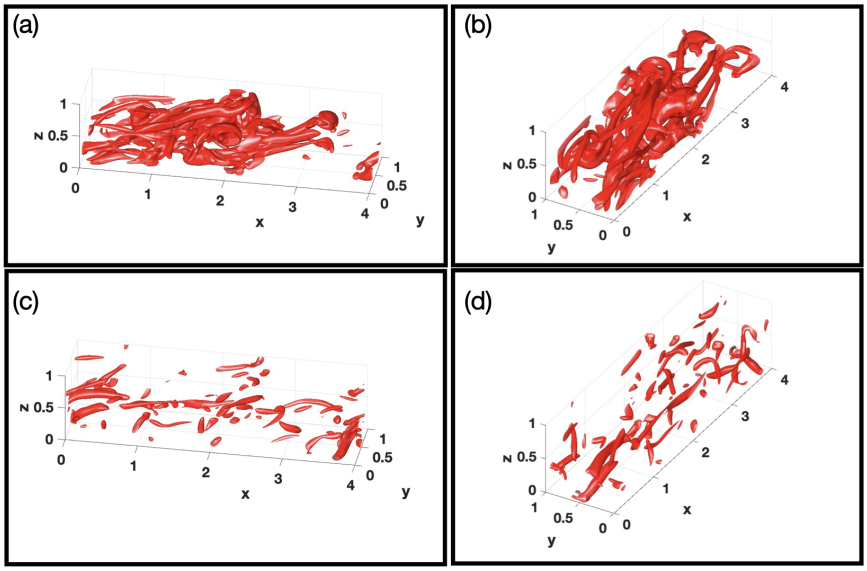

FIG. 8. Isosurfaces of the $Q = 0.025$ field indicating regions of coherent vortices. (a), (b) $\tau = 19.53$ from two different view points, (c),(d) $\tau = 27.34$ from two different view points.

ues of the enstrophy stretching term (i.e. vortex compression) are shown as magenta points, which theory suggests should fall in the second and fourth quadrants above the topological transition curve.

At $\tau = 19.53$ and 27.34 the maximum of vortex compression (the most negative value of ES) is 24% and 17% of the maximum vortex stretching (the largest positive value of ES). Moreover the the maximum vortex stretching (the largest positive value of ES) decreases by a factor of ten from $\tau = 19.53$ to 27.34. From Figures 10 and 11, it is observed that at both $\tau = 19.53$ and 27.34 the vortex compression follows the rule established for isotropic, homogeneous turbulence[26]. At $\tau = 27.34$ the extreme vortex stretching (green crosses) also falls in the correct quadrant. The flow yields more vortex stretching than compression, and a surprisingly high amount of this is associated with points in the second and third quadrants, and indeed even below the topological transition line. This effect is especially pronounced at $\tau = 19.53$ when the flow is most energetic, but still preserves some coherent vortical features (e.g. the vortex in the center of both panels of Figure 6).

C. Turbulence Decay and Maintenance

Table II compares the metrics of the vortex stretching (ES) and baroclinic production (EB) terms in the enstrophy equation over the mature 3D portion of the simulation. It can be seen that both in terms of maximum and mean the vortex stretching term dominates the baroclinic production. This is especially true for the peak KE_{3D} period near $\tau = 20$. At late times, the ratios are more comparable, but by $\tau = 27.34$ the vortex stretching term has dropped in magnitude by a factor of ten.

Throughout the fully three-dimensionalized period, ES and EB are positively correlated. However, the correlation never surpasses 0.25.

τ	$\frac{\max \lvert ES\rvert}{\max \lvert EB\rvert}$	$\frac{\text{mean } \lvert ES\rvert}{\text{mean } \lvert EB\rvert}$	correlation
19.53	9.49	7.62	0.21
23.44	6.85	3.76	0.16
27.34	5.69	2.27	0.24

TABLE II. Enstrophy budget terms metric comparison

The ability of the flow to maintain its fully three–dimensionalized state for late times is largely controlled by the enstrophy stretching term ES defined in equation (22). Because the flow is fully three-dimensionalized, patches of enstrophy occur throughout the computational domain. Figure 12 shows two isosurface of the enstrophy field. Since enstrophy is found to have sparsely distributed, strong peaks, isosurfaces at 10% and 20% of the maximum enstrophy are

ACCEPTED MANUSCRIPT
Physics of Fluids
AIP Publishing
This is the author's peer reviewed, accepted manuscript. However, the online version of record will be different from this version once it has been copyedited and typeset.
PLEASE CITE THIS ARTICLE AS DOI: 10.1063/5.0268302

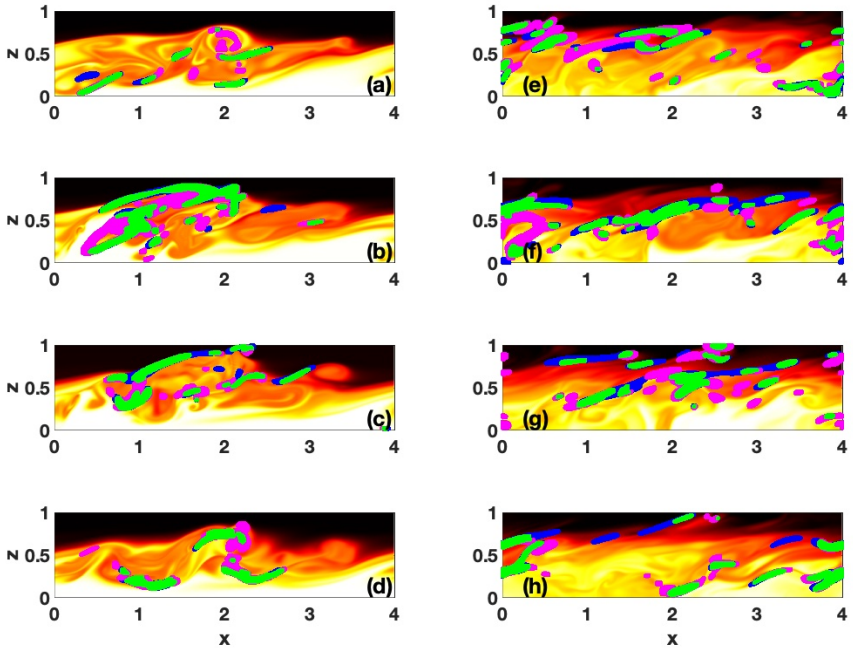

FIG. 9. Shaded plots of a slice of the temperature at $\tau = 19.53$ (a-d) and $\tau = 27.34$ (e-h). (a),(e) $y/L_y = 0.125$,(b),(f) $y/L_y = 0.375$, (c),(g) $y/L_y = 0.625$, (d),(h) $y/L_y = 0.875$. Superimposed on the plots are regions greater than 15% of the maximum value of viscous dissipation in magenta, and the vortex stretching and tilting term in blue. Regions with both quantities above their respective thresholds are shaded in green.

shown in panels (a) and (b), respectively. The isosurfaces are shaded by the enstrophy stretching term scaled by its absolute maximum value. Panel (a) shows that at 10% of the maximum enstrophy is fairly broadly distributed, however since most of the shading is dark green the majority of these isosurfaces do not experience strong stretching (regions in yellow experience weak vortex stretching). This can be contrasted with panel (b), in which the far more localized 20% of the maximum enstrophy iosurfaces are shown. It can be seen that the regions of strong enstrophy are aligned into streamwise streaks that are found below the interface between the unmixed near upper surface fluid and the main, mixed water column. The shading suggests that these high enstrophy regions experience strong stretching, implying that some amount of self–induced maintenance of the three–dimensional state is occurring.

The enstrophy tells a significant amount of the story of how the flow evolves, though it is important to note that the distribution of viscous dissipation matters as well. In order to explore this aspect of the flow, Figure 13 shows an isosurface of viscous dissipation at 20% of the maximum value of viscous dissipation. The isosurface clearly tracks the deformed shear layer, with additional patches at the two ends of the tank. The shading is once again the strength of the vortex stretching term. This shows that the deformed shear layer throughout the central portion of the domain experiences only weak vortex stretching, and hence slowly decays. However, some of the smaller patches of high viscous dissipation do experience strong vortex stretching. Future work should explore whether this local combination of enhanced vorticity and viscous dissipation significantly effects long time evolution.

IV. DISCUSSION, CONCLUSIONS AND FUTURE WORK

The results reported above suggest that despite the moderate Reynolds number and very low Atwood number, shear instability in the cold water regime achieves a state that is remarkably well-characterized by tools developed for fully de-

ACCEPTED MANUSCRIPT
Physics of Fluids
AIP Publishing
This is the author's peer reviewed, accepted manuscript. However, the online version of record will be different from this version once it has been copyedited and typeset.
PLEASE CITE THIS ARTICLE AS DOI: 10.1063/5.0268302

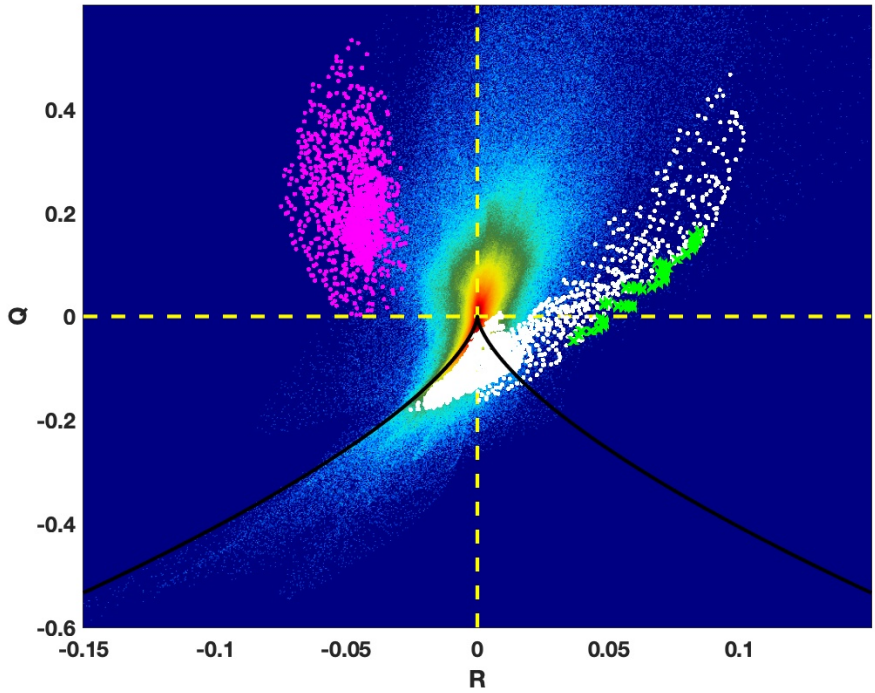

FIG. 10. The shaded $\log_{10}$ of the probability density in Q-R space, with colours saturated on $[-7,-4]$ for $\tau = 19.53$. The topological transition, $D = 0$, curve is superimposed in black. The 50% largest values of the enstrophy stretching term are shown as white points (top 10% further accentuated as green crosses). The 50% most negative values of the enstrophy stretching term (i.e. vortex compression) are shown as magenta points. The quadrants of Q-R space are denoted by dashed yellow lines.

veloped turbulence. In particular, the characterization in Q-R space proves quite accurate for both vortex stretching and compression.

The late time state is characterized by an active region beneath a relatively quiet region with little mixing of the temperature field. The enstrophy field experiences localized stretching that acts to preserve three-dimensional motions. These coincide with pre-existing regions of enstrophy, and thus the field is unable to fully break down the temperature stratification that develops near the upper boundary.

Both the coherent vortices (defined via the Q field) and the viscous dissipation field are marked by streamwise "worms". In the case of the viscous dissipation these are associated with a deformed shear layer (from $x = 1$ to $x = 3.5$ in Figure 13). Other less-coherent regions are observed as well (e.g., between $x = 3.5$ and $x = 4$ in the same figure). The large streamwise extent of the high dissipation regions prevents the development of an inertial subrange.

It is worth asking what role the weak buoyancy plays in the above described dynamics. To explore this a simulation was spawned from the base simulation at $\tau = 18.75$. For the new simulation $g = 0$ so that the density is a passive tracer, and buoyancy effects are not observed. Figure 14 shows the distribution of viscous dissipation, coloured by the enstrophy stretching and compression term, using the same parameters as Figure 13. It is immediately apparent that there is far less localization of the dissipation to the lower portion of the domain. The dissipation is more patchy, as opposed to a perturbed shear layer, and more regions of vortex stretching are evident

In order to get a sense of how the fully three-dimensionalized state is reached in the no buoyancy simulation, Figure 15 shows the evolution of temperature and its spanwise standard deviation, using the same convention as Figure 5 for the base case. It can be seen that at $\tau = 19.53$ the no buoyancy simulation is still quite similar to the base case.

ACCEPTED MANUSCRIPT
Physics of Fluids
AIP Publishing
This is the author's peer reviewed, accepted manuscript. However, the online version of record will be different from this version once it has been copyedited and typeset.
PLEASE CITE THIS ARTICLE AS DOI: 10.1063/5.0268302

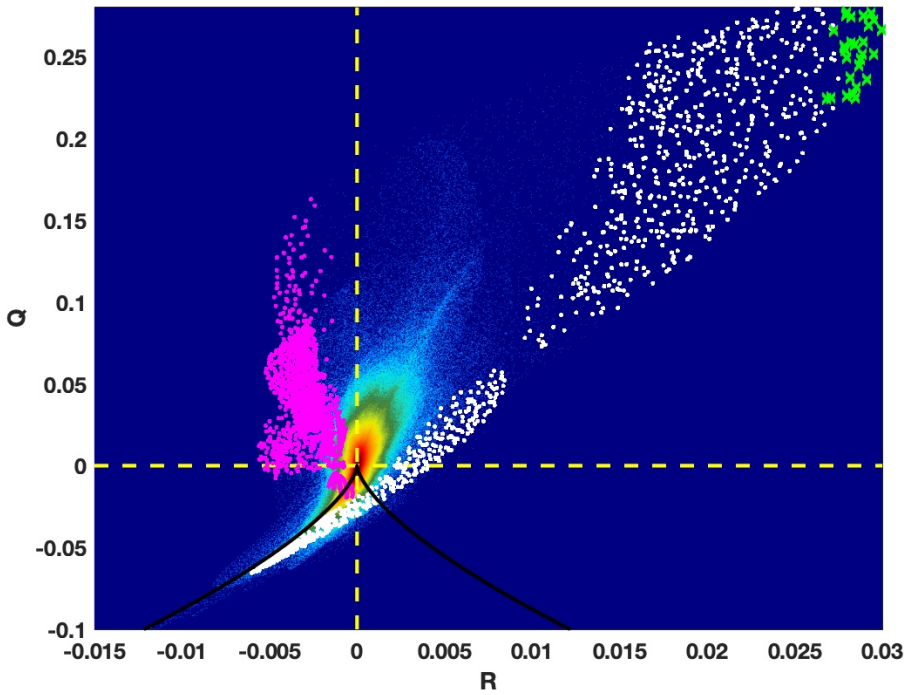

FIG. 11. *Q-R* Plot as in figure 10, but for $\tau = 27.34$. Note the change in axes extents

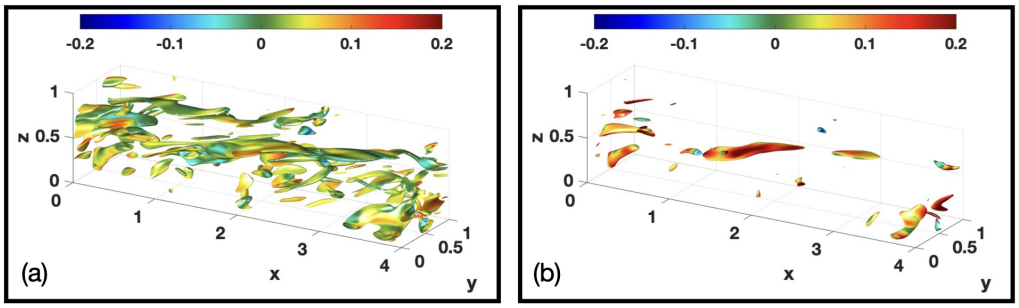

FIG. 12. (a) Isosurface of 10% of the maximum value of the enstrophy shaded by the enstrophy stretching term scaled by its maximum absolute value at $\tau = 27.34$. (b) Isosurface of 20% of the maximum value of the enstrophy shaded by the enstrophy stretching term scaled by its maximum absolute value at $\tau = 27.34$.

ACCEPTED MANUSCRIPT
Physics of Fluids
AIP Publishing
This is the author's peer reviewed, accepted manuscript. However, the online version of record will be different from this version once it has been copyedited and typeset.
PLEASE CITE THIS ARTICLE AS DOI: 10.1063/5.0268302

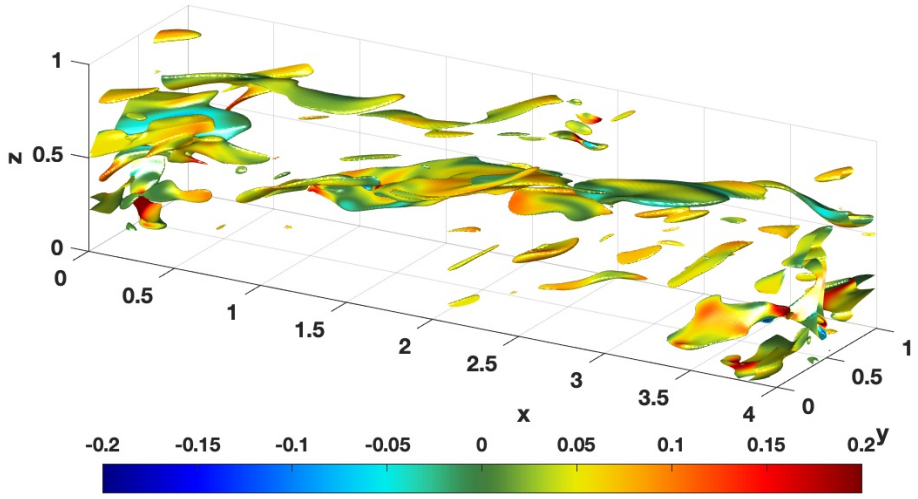

FIG. 13. Isosurface of 20% of the maximum value of the viscous dissipation shaded by the enstrophy stretching term scaled by its maximum absolute value at $\tau = 27.34$.

However by the $\tau = 23.43$ the zero buoyancy case has far larger spanwise standard deviations, and the layer of fluid near the upper boundary is at least partially mixed. By $\tau = 27.34$ this upper layer is completely mixed, in sharp contrast to the base case. Thus despite the fully three-dimensional nature of flow, and the inherently small density differences in the cold-water regime, buoyancy is essential to the quasi-turbulent dynamics.

An interesting question for future work is whether further organization of this mature state is possible when the unstable shear layer develops as part of a naturally occurring flow (e.g. an under-ice river outflow where the proximity of the interface to the boundary could influence the shear instability[31,32]). However, to address this question would require the construction of a parametrization scheme based on the state described in this work, as opposed to off-the-shelf eddy viscosity schemes.

A different avenue for future work, more focused on existing shear instability literature, would focus on how robust the cold-water results are for a more strongly stratified, faster moving fluid.

ACKNOWLEDGMENTS

This research project was funded by the Natural Sciences and Engineering Research Council of Canada (NSERC) Discovery Grant RGPIN-311844-37157.

DATA AVAILABILITY STATEMENT

During peer review data and analysis routines are available by request. A subset of the numerical simulations corresponding to the final version of the work will be archived in the Borealis data repository.

[1]B. Yang, J. Young, L. Brown, and M. Wells, "High-frequency observations of temperature and dissolved oxygen reveal under-ice convection in a large lake," Geophysical Research Letters **44**, 12–218 (2017).

ACCEPTED MANUSCRIPT
Physics of Fluids
AIP Publishing
This is the author's peer reviewed, accepted manuscript. However, the online version of record will be different from this version once it has been copyedited and typeset.
PLEASE CITE THIS ARTICLE AS DOI: 10.1063/5.0268302

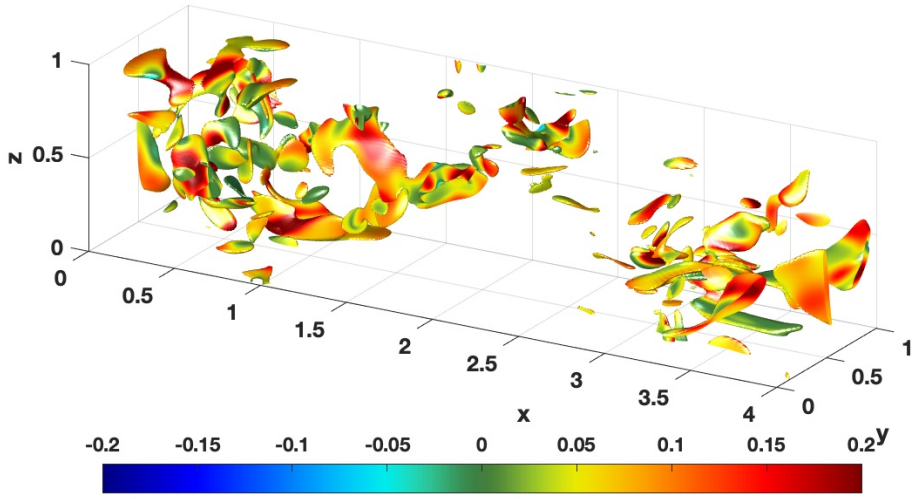

FIG. 14. Isosurface of 20% of the maximum value of the viscous dissipation shaded by the enstrophy stretching term scaled by its maximum absolute value at $\tau = 27.34$. The case shown has $g = 0$ from $\tau = 18.75$ and this figure should be contrasted with Figure 13.

[2]D. J. Allum, A. P. Grace, and M. Stastna, "Two-dimensional simulations of flow in ice-covered lakes with horizontal variations in surface albedo," Physical Review Fluids **7**, 103501 (2022).
[3]D. J. Allum and M. Stastna, "Simulations of buoyant flows driven by variations in solar radiation beneath ice cover," Physical Review Fluids **9**, 063501 (2024).
[4]Y. Chang and A. Scotti, "Flow structure of radiatively driven convection in inertial and rotating frames under steady and periodic radiative forcing," Physical Review Fluids **9**, 113503 (2024).
[5]C. P. Caulfield and W. R. Peltier, "The anatomy of the mixing transition in homogeneous and stratified free shear layers," Journal of Fluid Mechanics **413**, 1–47 (2000).
[6]Kundu, Piyush, *Fluid Mechanics* (Elsevier, 2016).
[7]R. T. Pierrehumbert and S. E. Widnall, "The two- and three-dimensional instabilities of a spatially periodic shear layer," Journal of Fluid Mechanics **114**, 59 (1982).
[8]G. P. Klaassen and W. R. Peltier, "The effect of prandtl number on the evolution and stability of Kelvin—Helmholtz billows," Geophysical & Astrophysical Fluid Dynamics **32**, 23–60 (1985).
[9]H. Salehipour, W. Peltier, and A. Mashayek, "Turbulent diapycnal mixing in stratified shear flows: the influence of prandtl number on mixing efficiency and transition at high reynolds number," Journal of Fluid Mechanics **773**, 178–223 (2015).
[10]W. R. Peltier and C. P. Caulfield, "Mixing efficiency in stratified shear flows," Annual Review of Fluid Mechanics **35**, 135–167 (2003).
[11]S. G. Monismith, J. R. Koseff, and B. L. White, "Mixing efficiency in the presence of stratification: When is it constant?" Geophysical Research Letters **45**, 5627–5634 (2018).
[12]E. C. Carmack, C. B. Gray, C. H. Pharo, and R. J. Daley, "Importance of lake-river interaction on seasonal patterns in the general circulation of kamloops lake, british columbia," Limnology and Oceanography **24**, 634–644 (1979).
[13]E. Carmack and S. Vagle, "Thermobaric processes both drive and constrain seasonal ventilation in deep great slave lake, canada," Journal of Geophysical Research: Earth Surface **126**, e2021JF006288 (2021).
[14]T. Hanson, M. Stastna, and A. Coutino, "Stratified shear instability in the cabbeling regime," Physical Review Fluids **6**, 084802 (2021).
[15]V. S. Mikhailenko, E. E. Scime, and V. V. Mikhailenko, "Stability of stratified flow with inhomogeneous shear," Physical Review E—Statistical, Nonlinear, and Soft Matter Physics **71**, 026306 (2005).
[16]A. P. Grace, A. Fogal, and M. Stastna, "Restratification in late winter lakes induced by cabbeling," Geophysical Research Letters **50**, e2023GL103402 (2023).
[17]G. Kirillin, M. Leppäranta, A. Terzhevik, N. Granin, J. Bernhardt, C. Engelhardt, T. Efremova, S. Golosov, N. Palshin, P. Sherstyankin, G. Zdorovennova, and R. Zdorovennov, "Physics of seasonally ice-covered lakes: a review," Aquatic Sciences **74**, 659–682 (2012).

AIP Publishing Physics of Fluids ACCEPTED MANUSCRIPT
This is the author's peer reviewed, accepted manuscript. However, the online version of record will be different from this version once it has been copyedited and typeset.
PLEASE CITE THIS ARTICLE AS DOI: 10.1063/5.0268302

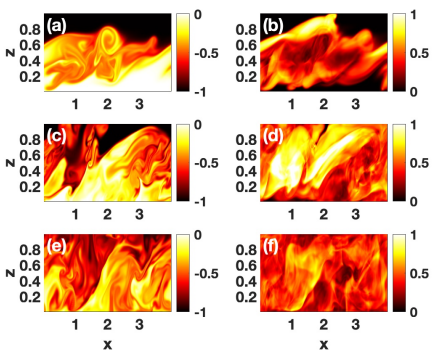

FIG. 15. Left column: slices of the temperature at $y = 0.074$, Right column: standard deviation of the temperature field. (a),(b) $\tau = 19.53$, (c),(d) $\tau = 23.43$, (e),(f) $\tau = 27.34$. The case shown has $g = 0$ from $\tau = 18.75$ and this figure should be contrasted with Figure 5. (a,c,e) have been scaled to lie on $[-1, 0]$ as in Figure 1, (b,d,f) have been scaled to lie on $[0, 1]$. All panels thus show the geometric distribution.

[18]N. Castro-Folker, A. P. Grace, and M. Stastna, "Three-dimensional structure of cold-water gravity currents," Physical Review Fluids **8**, 113901 (2023).
[19]K. Bhavsar, M. Stastna, and N. Castro-Folker, "Effects of buoyancy on shear instabilities in cold water," Submitted to Physical Review Fluids.
[20]W. Smyth and J. Moum, "Marginal instability and deep cycle turbulence in the eastern equatorial pacific ocean," Geophysical Research Letters **40**, 6181–6185 (2013).
[21]Q. Zhou, "Threshold behavior of local gradient richardson number in strongly stratified nonequilibrium turbulence," Physical Review Fluids **7**, 104802 (2022).
[22]C. J. Subich, K. G. Lamb, and M. Stastna, "Simulation of the Navier–Stokes equations in three dimensions with a spectral collocation method," International Journal for Numerical Methods in Fluids **73**, 103–129 (2013).
[23]D. Brydon, S. Sun, and R. Bleck, "A new approximation of the equation of state for seawater, suitable for numerical ocean models," Journal of Geophysical Research **104**, 2156–2202 (1999).
[24]W. D. Smyth, G. P. Klaassen, and W. R. Peltier, "Finite amplitude holmboe waves," Geophysical & Astrophysical Fluid Dynamics **43**, 181–222 (1988).
[25]H. Salehipour, W. Peltier, and A. Mashayek, "Turbulent diapycnal mixing in stratified shear flows: the influence of prandtl number on mixing efficiency and transition at high reynolds number," Journal of Fluid Mechanics **773**, 178–223 (2015).
[26]P. Davidson, *Turbulence: an introduction for scientists and engineers* (Oxford university press, 2015).
[27]A. Ooi, J. Martin, J. Soria, and M. S. Chong, "A study of the evolution and characteristics of the invariants of the velocity-gradient tensor in isotropic turbulence," Journal of Fluid Mechanics **381**, 141–174 (1999).
[28]M. S. Chong, A. E. Perry, and B. J. Cantwell, "A general classification of three-dimensional flow fields," Physics of Fluids A: Fluid Dynamics **2**, 765–777 (1990).
[29]H. Salehipour, W. R. Peltier, and C. P. Caulfield, "Self-organized criticality of turbulence in strongly stratified mixing layers," Journal of Fluid Mechanics **856**, 228–256 (2018).
[30]S. G. Hartharn-Evans, M. Stastna, and M. Carr, "A new approach to understanding fluid mixing in process-study models of stratified fluids," Nonlinear Processes in Geophysics **31**, 61–74 (2024).
[31]C.-L. Liu, A. K. Kaminski, and W. D. Smyth, "The effects of boundary proximity on Kelvin–Helmholtz instability and turbulence," Journal of Fluid Mechanics **966**, A2 (2023).
[32]J. T. Holt, "Experiments on Kelvin-Helmholtz billows influenced by boundaries," Geophysical & Astrophysical Fluid Dynamics **89**, 205–233 (1998).